# CHEMISTRY
## A European Journal

www.chemeurj.org


Reprint

A Journal of
ChemPubSoc Europe
ACES
Asian Chemical Editorial Society
WILEY-VCH

ChemPubSoc Europe

DOI: 10.1002/chem.201700914

CHEMISTRY A European Journal Full Paper

Supercapacitors

# Boron-Doped Polygonal Carbon Nano-Onions: Synthesis and Applications in Electrochemical Energy Storage

Olena Mykhailiv,[a] Krzysztof Brzezinski,[a] Bogdan Sulikowski,*[b] Zbigniew Olejniczak,[c] Malgorzata Gras,[d] Grzegorz Lota,[d] Agustin Molina-Ontoria,[e] Michal Jakubczyk,[f] Luis Echegoyen,*[g] and Marta E. Plonska-Brzezinska*[a]

**Abstract:** Doping of carbon nanostructures with heteroatoms, such as boron or nitrogen, is one of the most effective ways to change their properties to make them suitable for various applications. Carbon nano-onions (CNOs) doped with boron (B-CNOs) were prepared by annealing (1650 °C) nanodiamond particles (NDs) under an inert He atmosphere in the presence of B. Their physicochemical properties were measured using transmission (TEM) and scanning (SEM) electron microscopy, X-ray photoelectron spectroscopy (XPS), $^{10}B$ and $^{11}B$ solid-state magic-angle spinning (MAS) NMR spectroscopy, X-ray powder diffraction (XRD), Raman spectroscopy, porosimetry, and differential-thermogravimetric analyses (TGA-DTG). These properties were systematically discussed for the undoped and B-doped CNO samples. The amount of substitutional B in the CNO samples varied from 0.76 to 3.21 at.%. The TEM, XRD, and Raman analyses revealed that the increased amount of B doping resulted in decreased interlayer spacing and polygonization of the structures, which in turn led to their unusual physicochemical properties. All synthesized materials were tested as electrodes for electrochemical capacitors. The B-CNOs with low concentration of doping agent exhibited higher reversible capacitances, mainly owing to the formation of hydrophilic polygonal nanostructures and higher porosity.

## Introduction

Carbon nano-onions (CNOs) consist of a hollow spherical fullerene core surrounded by concentric spherical graphene layers.[1] The temperature annealing of ultradispersed nanodiamond (ND) particles of approximately 5 nm average diameter results in the formation of CNOs consisting of a few graphene shells (6–8 layers).[2,3] Recent studies revealed that the spherical onion-like structures are superior to other carbon nanostructures (CNs)[4,5] in terms of thermal stability, reactivity, and conductivity. Owing to their promising properties, CNO materials are being used in a variety of carbon electrodes.[5,6] One of the proposed solutions to control the electronic properties of CNs is to dope them with donors or acceptors. Many elements such as B, P, N, S, and halogens are potential dopants that can improve the electronic performance of CNs.[7] Doping of materials is the most common method to fabricate integrated circuits with applications in nanooptics, nanoelectronics, and photovoltaic devices.[8,9] In particular, doping certain kinds of heteroatoms into the CNs can form electron-excess n-type or electron-deficient p-type (e.g., B-doped CNs) materials.[10,11]

Owing to its oxidation resistance, B is one of the most frequently studied elements. It enters the carbon lattice by substituting carbon atoms and acts as an electron acceptor because it only contains three valence electrons. This causes a shift in the Fermi level towards the conduction band and a modification of the electronic structure of the carbon structures.[12,13] B has been used as a dopant in carbon and diamond materials to affect their electrochemical properties.[14] Doping with B improves field-emission properties when compared with pristine CNs.[15] Sometimes such nanostructures behave as superconductors.[16] B-doped CNs therefore show large photoconductivities[17] as well as catalytic effects toward many oxygen-contain-

[a] O. Mykhailiv, Dr. K. Brzezinski, Prof. M. E. Plonska-Brzezinska
Institute of Chemistry, University of Bialystok
Ciolkowskiego 1 K, 15-245 Bialystok (Poland)
E-mail: mplonska@uwb.edu.pl

[b] Prof. B. Sulikowski
Jerzy Haber Institute of Catalysis and Surface Chemistry, Polish Academy of Sciences
Niezapominajek 8, 30-239 Cracow (Poland)
E-mail: ncsuliko@cyf-kr.edu.pl

[c] Prof. Z. Olejniczak
Institute of Nuclear Physics, Polish Academy of Sciences
Radzikowskiego 152, 31-342 Cracow (Poland)

[d] M. Gras, Dr. G. Lota
Poznan University of Technology, Institute of Chemistry and Technical Electrochemistry
Berdychowo 4, 60-965 Poznan (Poland)

[e] Dr. A. Molina-Ontoria
IMDEA Nanoscience, C/Faraday
9 Ciudad Universitaria de Cantoblanco 28049, Madrid (Spain)

[f] Dr. M. Jakubczyk
Faculty of Chemistry, Warsaw University of Technology
Noakowskiego 3, 00-664 Warsaw (Poland)

[g] Prof. L. Echegoyen
Department of Chemistry, University of Texas at El Paso
500 W. University Ave., El Paso, TX 79968 (USA)
E-mail: echegoyen@utep.edu

Supporting Information for this article can be found under: https://doi.org/10.1002/chem.201700914.

ing species.[7,18] Thus, they can be used as gas sensors (CO, $H_2$).[19]

To our best knowledge, only a few articles have been published so far dwelling on doping of CNOs by heteroatoms such as N[20] and B.[21] In these studies, however, the direct chemical modification of the external graphene layers was performed by using aggressive reagents, which led to the destruction of the π-conductive surfaces. The possibility to dope CNOs during their actual synthesis, rather than through a post-synthetic treatment, constitutes an attractive method. The first report involving the direct preparation of CNOs in the presence of a B source ($H_3BO_3$) was published recently.[22] The structures of the onion-like carbon nanotubes proved to be highly defective. In this article, we demonstrate an effective procedure for doping the CNOs with B by annealing the former with NDs. As a result, the B-containing CNOs were prepared with the retained graphitic-layer structures. Such behavior seems to be of paramount importance for keeping their high conductivity as well as other desirable properties.

## Results and Discussion

B atoms were introduced into the CNO structures by annealing of CNOs with NDs under an inert He atmosphere. Commercially available NDs with a crystal size between 4 and 6 nm were used for the preparation of doped CNOs.[2] The central fullerene at the core of the CNOs was surrounded by multiple layers of nested concentric graphitic shells, with an intershell spacing estimated from the high-resolution transmission electron microscopy (HRTEM) diffraction patterns of approximately 0.34 nm,[23,24] similar to that for highly oriented pyrolitic graphite (HOPG).[25] The standard procedure revealed spherical nanostructures composed of 6–11 layered CNOs.[26]

The doping process occurring during the formation of these nanostructures led to a high degree of polygonization of the spherical structures of the CNOs (i.e., a faceting structure as marked in Figure 1 a and b).[27] The TEM diffraction patterns also indicated that the intershell interactions in pristine CNOs were much weaker compared to those found in B-CNOs (inset in Figure 1 a), the latter showing interlayer distances of approximately 0.28 nm. B-doping led to an increase in graphitization of the CNOs. The SEM images of a gold foil covered with the doped CNOs are shown in Figure 1 c–e. The morphology of the B-doped CNOs differed markedly (Figure 1 a), and the structures exhibited porous morphologies with numerous channels and outcroppings. All samples were composed of aggregates of the nanoparticles of sizes below 4 μm; however, the average carbon-particle size increased with the amount of B used in the starting materials. The 3B-CNO derivatives formed spherical aggregates with a diameter size of approximately 2–4 μm (Figure 1 e). The 1B-CNO particles formed more uniform structures, consisting of smaller 1 μm nanoparticles (Figure 1 c). We observed sheet-like regions (marked in Figure 1 d and e) of constant contrast, which probably indicate domains of inorganic components ($B_2O_3$). We noted that the amount of these domains increased with the amount of B in the starting materials.

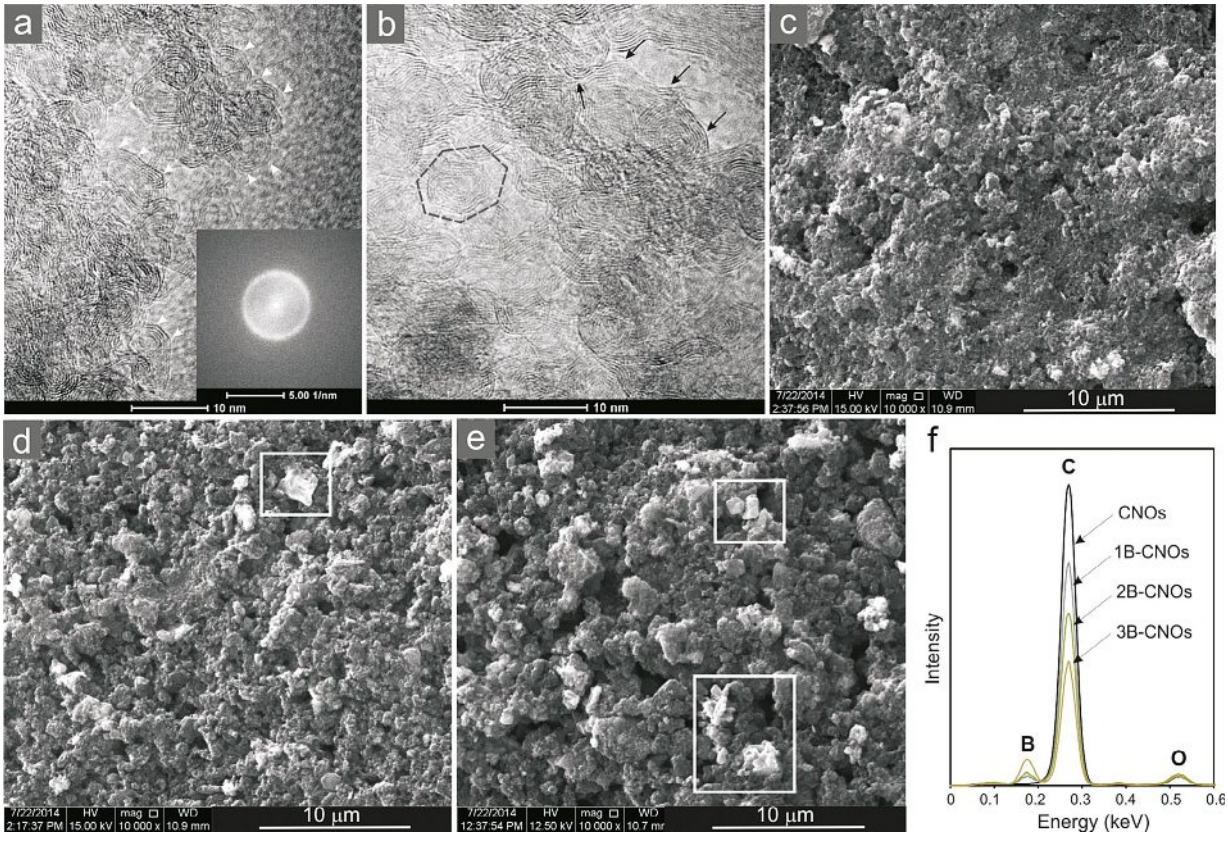


**Figure 1.** (a, b) TEM and (c, d, e) SEM images of (a, c) 1B-CNOs, (b, d) 2B-CNOs, and (e) 3B-CNOs. (f) EDX analysis of B-CNOs with different mass ratios of NDs and B in the synthesis procedure.

The energy dispersive X-ray (EDX) spectra (Figure 1 f) of B-CNOs revealed that the materials contained C, B, and O, with different mass ratios of C and B. The series depicted in Figure 1 f also indicates a trend of increasing B amount in the B-CNOs with increasing the B content in the pristine material.

X-ray diffraction (XRD) studies showed a gradual transformation of diamond to graphite as a function of B doping. XRD patterns of pristine NDs, undoped CNOs, and B-doped CNOs are shown in Figure 2. The ND profile revealed the presence of

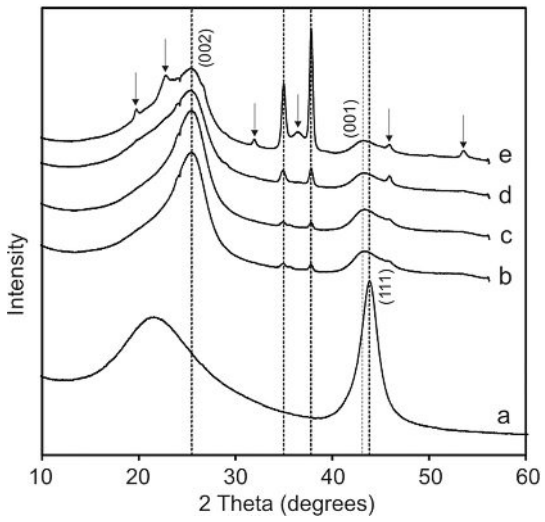


**Figure 2.** XRD patterns of (a) NDs, (b) CNOs, (c) 1B-CNOs, (d) 2B-CNOs, and (e) 3B-CNOs.

a mixture of various phases. In ND materials, the strongest reflection around $2\theta = 43.8^\circ$ corresponded to the (111) basal-plane diffraction of the diamond structure (Figure 2 a).[28] A certain amount of a graphite-like and an amorphous phase ($2\theta = 21.5^\circ$) was also found.[29,30] The conversion from NDs to the graphitized CNOs was observed during the annealing process of the starting material. For all patterns, an asymmetric broad reflection in the range between 23–27° and a second one with a maximum at 43.0° were observed. They were attributed to the (002) and (100) planes of graphite, respectively (Figure 2 b–e). The broad signal centered around 23–27° suggests the contribution of some $sp^2$-bonded carbons in the CNO samples and can be assigned to two separate forms of carbon, turbostratic carbon (amorphous) and graphene carbon (graphitic carbon).[31] This signal was relatively broad and weak in intensity if the B content was higher. The diffraction broadening arose primarily from the size of the nanoparticles, but it could also arise from strains and defects present in the crystal material itself or from the incompletely formed shells of CNOs. All profiles of the B-doped CNOs showed the presence of small peaks at 19.6, 22.6, 31.5, 36.0, 45.5, and 53.2° (marked peaks in Figure 2 e). Finally, the two strongest reflections at 35.1 and 37.8° (Figure 2 e) corresponded to a graphitic phase[32] and boron carbide.[33,34]

Quantitative studies were performed using X-ray photoelectron spectroscopy (XPS). The survey spectra for the undoped CNOs and B-CNOs samples are compared in Figure SI1 in the Supporting Information, and their elemental quantification is summarized in Table SI1 in the Supporting Information. The XPS spectra contained one peak (C 1 s) for CNOs and four peaks (B 1 s, C 1 s, N 1 s, and O 1 s) for B-CNOs, respectively (Figure SI1 in the Supporting Information). A deconvolution of the high-resolution C 1 s spectrum for the undoped CNOs showed a main $sp^2$-hybridized carbon peak located at 284.5 eV and a minor $sp^3$-hybridized carbon peak located at 285.1 eV.[35,36] The position of the C 1 s peak (at 284.5 eV; graphitic C) varied with the degree of B doping. We found that the C 1 s peak was downshifted by 0.15 eV in B-doped CNOs, in agreement with the results obtained for B-doped graphite (Figure SI2 in the Supporting Information).[37,38] A downshift in the binding energy and a slight increase in the full width at half-maximum (FWHM) intensity were detected for the C 1 s peak of the boron atoms in CNOs (Table SI1 in the Supporting Information). This observation can be rationalized by the lowering of the Fermi level owing to the formation of a chemical bond between C and B.[37] The C 1 s spectrum of B-doped CNOs could be deconvoluted into five peaks at 283.0, 284.5, 285.1, 286.6, and 290.1 eV, which were assigned to the C–B, C–C (graphitic $sp^2$-C), C–C ($sp^3$-C), C–N, and C–O bonds, respectively (Table SI1 and Figure SI2 in the Supporting Information).

The XPS data for B-CNOs revealed another peak at approximately 190 eV corresponding to the B 1 s spectrum (Figure 3). The shift of the B 1 s signal toward higher binding energy compared to that of elemental B (≈187.7 eV) indicates substitution of the B atoms into the $sp^2$-carbon network (Table SI1 in the Supporting Information). A detailed line-shape analysis was performed for the B 1 s peak to better understand various contributions (Figure 3). The XPS studies showed that in the doped CNOs, B–C bonds (187.5–189.5 eV), B–O bonds (191–193 eV), and B–N bonds (188–191 eV) were present.[37,39] As shown in Figure 3, the B 1 s core signal for 1B-CNOs could be deconvoluted into peaks at 189.0 ($B_{sub}$–C bond, indicating substitution of B in CNOs), 190.6 (the planar $BC_3$ nanodomain and/or the B–O bond in $BC_2O$), and 192.0 eV, corresponding to the presence of N in the CNO nanostructures (Table SI1 in the Supporting Information).[38,39] The signals at 193.5 and 194.6 eV were most likely results of the residual B–O ($B_2O_3$). The presence of $B_2O_3$ can be explained by the oxidation of unreacted B in the post-annealing process. The level of doping by B (Table SI1 in the Supporting Information) was determined from the areas under the C 1 s, N 1 s, O 1 s, and B 1 s peaks. As expected, the B content increased with the relative amount of B used in the CNO syntheses. The amount of substitutional B in CNOs, determined from the total B concentration, was 0.76 (1B-CNOs), 1.6 (2B-CNOs), and 3.21 at.% (3B-CNOs).

B NMR spectroscopy is frequently used to monitor the chemical environment of B in various materials, including elemental B,[40] B compounds,[41] oxides,[42] glasses,[43] and zeolites.[44,45] There are two B isotopes with nuclear spins: $^{11}B$ and $^{10}B$, with natural abundances of approximately 80 and 20%, respectively. The corresponding spins are equal to 3/2 and 3, and the quadrupolar moment of $^{10}B$ is two times larger than that of $^{11}B$. The magic-angle spinning (MAS)-NMR spectrum of

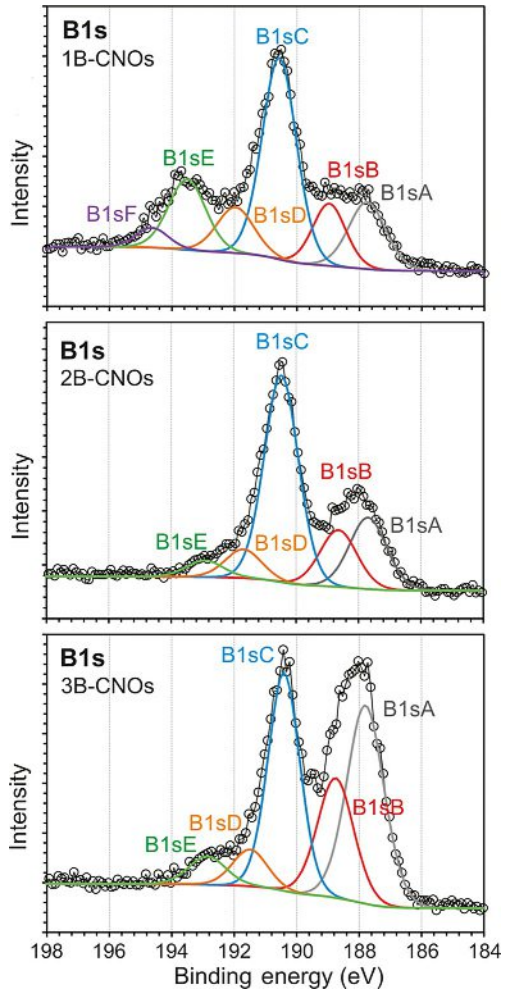


**Figure 3.** XPS spectra of B 1s signals of the B-doped CNOs.

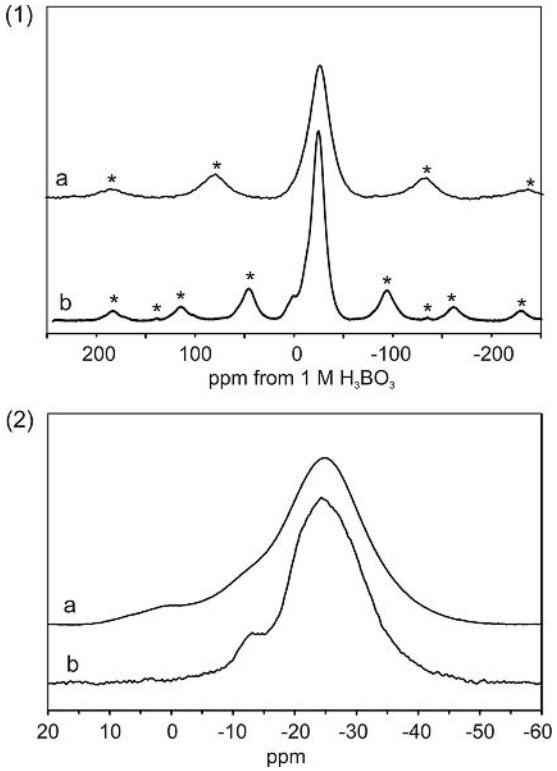


**Figure 4.** (1) $^{11}$B MAS NMR spectra of 3B-CNOs (a) at 96.2 MHz and (b) at 160.5 MHz. Spinning speed was 11 kHz, and the asterisks denote spinning side-bands. (2) A comparison of B NMR spectra of the 3B-CNOs sample: (a) $^{11}$B MAS NMR at 160.5 MHz and (b) $^{10}$B MAS NMR at 53.7 MHz.

the half-integer $^{11}$B is affected by the second-order quadrupolar interaction. In the case of $^{10}$B, the first-order quadrupolar interaction is dominant and causes a wide spread of signal intensities over the spinning sidebands. For these reasons, $^{10}$B NMR is rarely used.[46,40]

For the sample containing the highest amount of boron (3B-CNOs), the $^{11}$B MAS-NMR spectra were acquired at two different frequencies, 96.2 and 160.5 MHz. The $^{11}$B spectrum recorded at the lower field is depicted in Figure 4a, panel (1). This spectrum is dominated by a major signal at approximately −24 ppm, which is surrounded by a series of spinning sidebands. Because the magnitude of the second-order quadrupolar interaction is inversely proportional to the value of the magnetic field, more details are revealed in the spectrum at higher fields; in particular, a new signal at 0.3 ppm appears [Figure 4b, panel (1)]. Moreover, upon close inspection of the spectrum, an additional signal can be discerned as a broad shoulder at approximatel −11 ppm [Figure 4a, panel (2)].

To obtain more information on the system studied, the $^{10}$B spectrum was also acquired at 53.7 MHz [Figure 4b, panel (2)]. In comparison with the $^{11}$B spectrum, the signal at −11 ppm was better resolved. However, the signal at 0 ppm disappeared completely. Both B isotopes are quadrupolar, and the strength of the quadrupole interaction is characterized by the quadrupole coupling constant ($C_Q$), whereas the asymmetry parameter $\eta$ is a measure of the departure from the electric-field gradient (EFG) from axial symmetry. Because in the $^{10}$B spectrum the signal at 0 ppm disappeared, it can be concluded that the B-site resonance at 0 ppm exhibits a much larger $C_Q$ than the signals at −13 and −24.3 ppm. Such a situation is encountered owing to distribution of the $^{10}$B signal intensity over the spinning sidebands according to the ratio $C_Q/\nu_{MAS}$, in which $\nu_{MAS}$ denotes the sample spinning speed. Using a model B compound ($Na_2B_4O_7{\cdot}10H_2O$, borax) a similar decrease of the $^{10}$B signal was observed experimentally.[46] Information retrieved from the 1-dimensional (1D) $^{11}$B and $^{10}$B MAS NMR spectra can be summarized as follows. For the B-CNOs, three B sites are present at approximately. 0, −11, and −24 ppm (Table 1). The signal at 0 ppm, which is completely absent for the $^{10}$B spectrum [Figure 4b, panel (2)], can be assigned to trigonal B sites (B atoms doped into CNOs). The signals at approximately −11 and −24 ppm, seen both in the $^{11}$B and the $^{10}$B spectra, are caused by tetrahedrally coordinated B sites. In Figure 5, the $^{11}$B spectra for the three samples are shown. Three lines are present in all samples. The spectra were deconvoluted assuming Gaussian line shapes, and the results are listed in Table 1. In all samples, the dominant signals were located at approximately −24 ppm. Interestingly, the signals at −11 ppm did not change with the B content, whereas the signals in the 0–1 ppm range increased upon decreasing the amount of B.

**Table 1.** Chemical shift and Gaussian deconvolution[a] of the $^{11}B$ MAS NMR spectra acquired at 160.5 MHz.

| Sample | Chemical shift [ppm] | Signal intensity [%] |
|---|---|---|
| 1B-CNOs | 0.6 | 18.39 |
| | −11.3 | 4.00 |
| | −24.1 | 77.61 |
| 2B-CNOs | 0.9 | 15.44 |
| | −10.8 | 5.96 |
| | −24.2 | 78.60 |
| 3B-CNOs | 0.3 | 7.49 |
| | −11.2 | 6.43 |
| | −24.6 | 86.08 |

[a] Correlation coefficient *R* better than 98%.

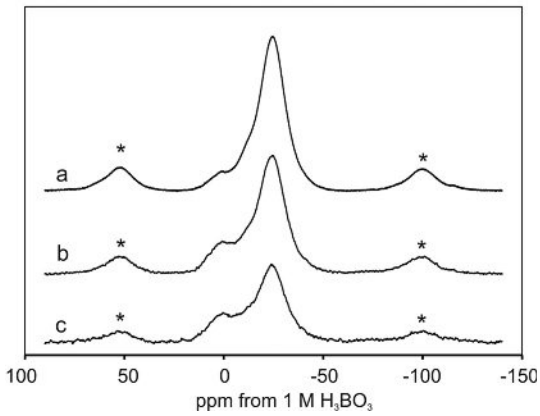


**Figure 5.** $^{11}B$ MAS NMR spectra, acquired at 160.5 MHz, of (a) 3B-CNOs, (b) 2B-CNOs, and (c) 1B-CNOs. Spinning speed was 12 kHz, and the asterisks denote spinning side-bands.

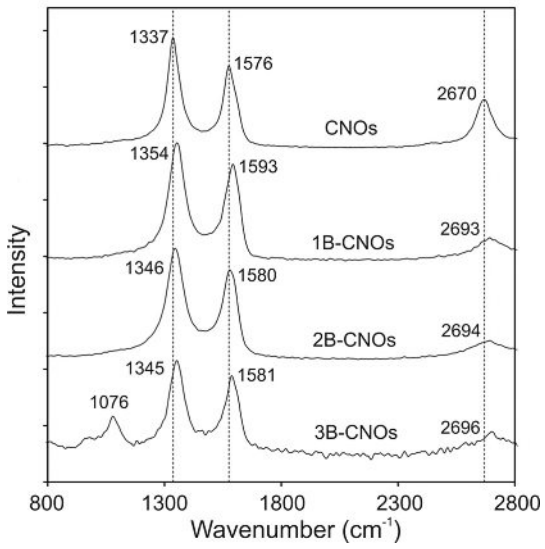


**Figure 6.** Raman spectra (recorded at $\lambda_{ext}=514$ nm) of CNOs, 1B-CNOs, 2B-CNOs, and 3B-CNOs.

**Table 2.** Best-fit frequencies for *D* and *G* bands obtained at 514 nm laser excitation energies and relative intensity $I_D/I_G$.

| Sample | *D* band [$cm^{-1}$] | *G* band [$cm^{-1}$] | *2D* band [$cm^{-1}$] | $I_D/I_G$ |
|---|---|---|---|---|
| CNOs | 1337 | 1576 | 2670 | 1.33 |
| 1B-CNOs | 1354 | 1593 | 2693 | 1.36 |
| 2B-CNOs | 1346 | 1580 | 2694 | 1.44 |
| 3B-CNOs | 1345 | 1581 | 2696 | 1.43 |

The Raman spectra of CNOs showed three main features in the 1000–3000 $cm^{-1}$ region: a *G* band (≈1575 $cm^{-1}$), the disorder-induced *D* band (≈1335 $cm^{-1}$), and the highly dispersive second-order harmonic of the *2D* band (≈2670 $cm^{-1}$). The Raman spectra of pristine and B-doped CNO samples at 514.5 nm are shown in Figure 6a, and the data are collected in Table 2. The doping of the CNs affected the frequency of the C–C bond vibrational modes (*G* band). This band reflects the structural information of the hexagonal graphene plane of the carbon materials.[47] B-doping resulted in a characteristic *G* band upshift, which increased with the doping level of B.[31] The *G* band appeared at 1576 $cm^{-1}$ for CNOs (Figure 6a, spectrum 1) and shifted to 1593 $cm^{-1}$ for the 1B-CNOs (Figure 6a, spectrum 2; see also Table 2). The shift of this band is related to the expansion or contraction of the C–C bonds, owing to lattice defects arising from B doping.[48,31] The doping introduces holes in graphene sheets and promotes the electron transfer between valence and conduction bands, thus improving the electric conductance. Resonance Raman data are useful to monitor the perturbation of the sidewall π-electron density of CNs; the frequency of their vibrational bands is sensitive to the density of electrons in the CNs.[49] A displacement to higher/lower wavenumbers is related to the interaction of the CN with the electron acceptor/donor, respectively.[50]

The data for the three main bands showed that the vibrational bands of the B-CNOs shifted to higher wavenumbers, suggesting doping of the CNO cages with B (electron acceptor). It is important to note that the peak position of the *D* band changed from 1337 $cm^{-1}$ for the undoped sample to 1354 $cm^{-1}$ for the B-doped CNOs (1B-CNOs, Figure 6a). The same trend was observed for the 2B-CNO and 3B-CNO materials (Table 2). All samples also exhibited broad *2D* bands at approximately 2690 $cm^{-1}$. These bands were assigned to overtone scattering (ca. 1354 $cm^{-1}\times2$, 1346 $cm^{-1}\times2$, and 1345 $cm^{-1}\times2$). The *2D* band is an overtone of the *D* band and sensitive to changes in the electronic structure, such as those resulting from the incorporation of dopants.[51,52] The Raman spectrum for pristine CNOs showed the lowest *D*/*G* intensity ratio ($I_D/I_G=1.33$). B doping increased the intensity of the *D* band (1B-CNOs: $I_D/I_G=1.36$; 2B-CNOs: $I_D/I_G=1.38$; 3B-CNOs: $I_D/I_G=1.43$) as a result of the formation of the B–C network. The effect of B doping primarily led to a systematic increase in the intensity of the disorder-induced band (*D* band). This result is in accordance with previous results, indicating that the amount of disordered structures ($sp^3$) relative to the ordered structure (crystalline) increased with increasing B-doping concentration. To summarize, B doping of the CNOs leads to an increase of the *D* peak intensity and a shift of the *G* peak posi-

tion to higher wave numbers. This is the result of stronger clustering of $sp^2$-carbons and a shortening of the average C=C distance.[53]

To further confirm the successful doping of B atoms in the CNO cages, Fourier-transform (FT)-IR spectra of pristine CNOs and B-CNOs were collected (Figure SI3 in the Supporting Information). The IR absorption between approximately 1520 and 1540 $cm^{-1}$ is consistent with hexagonal C–C domains (Figure SI3 in the Supporting Information).[54] The two bands located at approximately 1220 and 1370 $cm^{-1}$ can be assigned to the out-of-plane B–C and the B–C–B in-plane bonding vibrations.[55] The IR band centered at 1220 results from the planar B–C units.[56] The signals at approximately 1370 $cm^{-1}$ can be attributed to B–N[57] or N–C stretching, C–C ring stretching, or asymmetric B–O stretching.[58]

It was of interest to estimate thermal stability of the undoped CNOs and B-CNOs in air, Ar, and $O_2$ atmospheres by derivatography. The temperature necessary for the removal of the amorphous carbon formed during the annealing of NDs in air is lower than the decomposition temperature of the pristine CNs. The onset of oxidation, inflection, and end temperatures are listed in Table SI2 in the Supporting Information, representing the initial weight loss, the maximum weight loss, and the final weight in the differential-thermogravimetric analysis (TGA-DTG) graphs, respectively. The lowest inflection temperature was observed for the pristine CNOs, $I_t = 650\,^{\circ}C$ (Table SI2 in the Supporting Information and Figure 7a, curve 1), with a total weight loss of 98% at 700 °C. The single sharp mass-loss transition corresponding to the combustion of CNOs signifies that the material is a homogeneous single phase with no other carbon-material impurities. According to the results presented by Chen et al.,[59] better graphitized CNs are obtained at higher oxidation temperatures. A higher inflection temperature was observed for the B-CNOs ($I_t = 680\,^{\circ}C$, air atmosphere) than for the pristine CNOs ($I_t = 650\,^{\circ}C$, air atmosphere) (Table SI2 in the Supporting Information). Additional studies in the $O_2$ atmosphere confirmed the formation of B oxide during the annealing process of B-CNOs (Figure 7, curves 5 and 6). In an inert atmosphere, we observed high thermal stability of both the CNOs and the B-CNOs up to 930 and 1050 °C, respectively (Table SI2 in the Supporting Information). These results confirmed the higher graphitization degree of the CNs upon doping with B. The percentage of the total B concentration (substituted and unsubstituted) can be estimated from the weight loss of the TGA curves. The mass ratios of total boron (substituted and unsubstituted) to CNOs calculated from the TGA studies (air atmosphere, Table SI2 in the Supporting Information), are similar to those determined from the XPS studies (Table SI1 in the Supporting Information).

The porosity, pore-size distribution, and specific surface areas all affect the specific capacitances of electrodes.[60,61] The adsorption and desorption characteristics of an inert gas, the micro- and mesopore structure, the pore volume, and the specific surface area of the CNO samples were determined using the BET static $N_2$ adsorption technique.[62] The samples were characterized by $N_2$ sorption isotherms at 77 K (Figure SI4 in the Supporting Information). The doping process resulted in

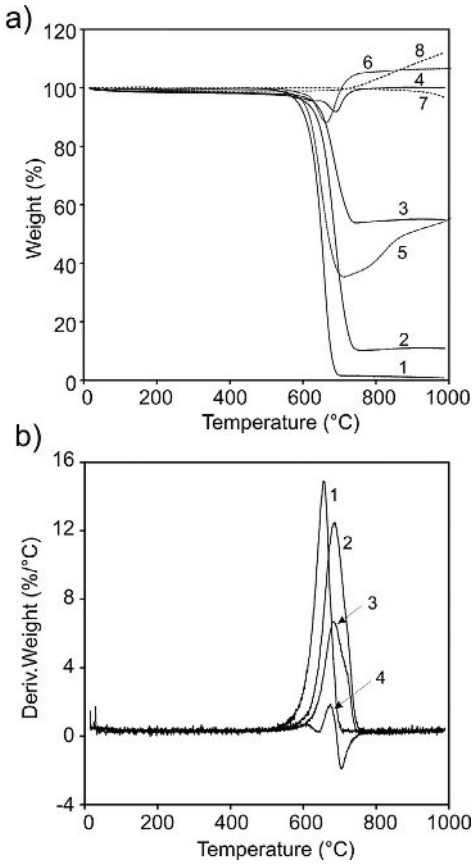


**Figure 7.** (a) TGA and (b) DTG curves for (1) CNOs, (2) 1B-CNOs, (3) 2B-CNOs, and (4) 3B-CNOs in air, (5, 6) $O_2$, and (7, 8) Ar atmosphere at 10 °C $min^{-1}$.

a remarkable reduction of $N_2$ adsorption, which is indicative of a decrease in the specific surface area ($S_{BET}$), external surface area ($S_{ext}$) (without microporous structures), and microporosity (Table 3). The specific surface areas were between 288 (1B-CNOs) and 205 $m^2 g^{-1}$ (3B-CNOs). Doping of the CNOs with B also resulted in a decrease of their microporosity (Table 3). An increase in the B content led to significant transformation of the CNO microstructures. The total surface area of the micropores decreased from 46 $m^2 g^{-1}$ (undoped CNOs) to 41 (1B-CNOs), 26 (2B-CNOs), and 16 $m^2 g^{-1}$ (3B-CNOs). The same tendency was observed for the total volume area of the micropores, decreasing from 1.559 (undoped CNOs) to 0.967 $cm^3 g^{-1}$ (3B-CNOs) (Table 3). To conclude, doping with B significantly affects the microporous/mesoporous structure of the carbon materials studied.

To explore the potential application of B-doped materials in energy-storage devices, the synthesized samples were used as supercapacitor electrodes and characterized by using cyclic voltammetry (CV), electrochemical impedance spectroscopy (EIS), and galvanostatic charge–discharge measurements in 1 mol $dm^{-3}$ $H_2SO_4$ aqueous solution.

CV measurements of the undoped and B-doped CNO electrodes performed in a three-electrode cell are visualized in Figure 8a. These electrodes were stable within the applied potential window, and all CV curves showed pseudo-rectangular profiles, indicating a nearly ideal double-layer capacitor (EDLC) be-

**Table 3.** Physicochemical parameters of CNOs, B-CNOs (1:10), B-CNOs (1:5), and B-CNOs (1:2).

| Sample | $S_{BET}$[a] [$m^2\,g^{-1}$] | $S_{ext}$[b] [$m^2\,g^{-1}$] | *t*-plot micropore area [$m^2\,g^{-1}$] | Pore volume $V_p$ [$cm^3g^{-1}$] | Average pore size [nm] |
|---|---|---|---|---|---|
| CNOs | 454 | 408 | 46 | 1.559[c] | 13 |
| B | 11 | 14 | n.d. | 0.017[d] | 6 |
| 1B-CNOs | 288 | 245 | 41 | 1.305[e] | 17 |
| 2B-CNOs | 237 | 211 | 26 | 1.103[f] | 16 |
| 3B-CNOs | 188 | 172 | 16 | 0.967[g] | 16 |

[a] $S_{BET}$ = BET specific surface area; [b] $S_{ext}$ = external surface area, based on *t*-plot. Single-point-adsorption total pore volume of pores less than [c] 1193 Å diameter at $p/p^0 = 0.9836$; [d] 1232 Å diameter at $p/p^0 = 0.9842$; [e] 1176 Å diameter at $p/p^0 = 0.9834$; [f] 1216 Å diameter at $p/p^0 = 0.9839$; [g] 1268 Å diameter at $p/p^0 = 0.9846$. n.d. = not determined.

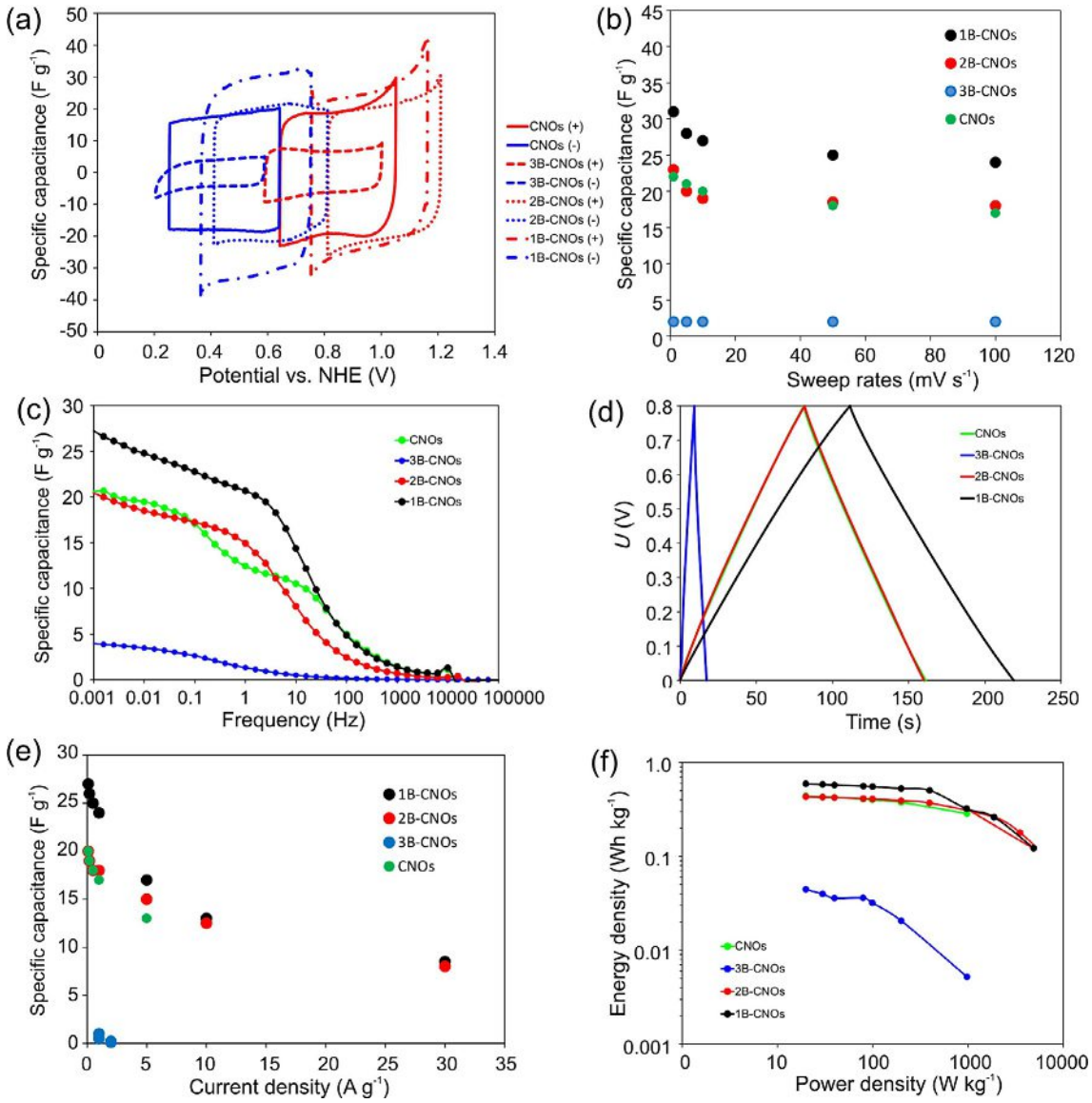


**Figure 8.** (a) CV at 5 mV $s^{-1}$ (three-electrode cell); (b) specific capacitance versus sweep rates (two-electrode cell); (c) specific capacitance versus frequency dependence; (d) galvanostatic charge–discharge curves at 100 mA $g^{-1}$ (two electrode cell); (e) specific capacitance versus current density; (f) Ragone plot.

havior.[60] It was found that doping increased the capacitance of both the negative and the positive electrodes. The capacitance of the negative electrode in the case of 1B-CNOs was higher than that of the positive one by 30 F $g^{-1}$. CNOs and the doped CNO nanostructures exhibited excellent capacitive behavior even under quick charge–discharge conditions (Fig-

ure 8b). There was a gradual decrease in the specific capacitance with increasing sweep rates. When the sweep rate was increased from 1 to 100 mV s$^{-1}$, the capacitive current decreased to approximately 80% of the starting value. Moreover, the specific capacitance of 1B-CNOs could reach values of approximately 30 F g$^{-1}$ for low sweep rates, which was almost completely retained after 5000 cycles. These results demonstrate convincingly that B-CNOs exhibit excellent cycling stability when used as the electrode materials for supercapacitors.

There is a clear correlation between the concentration of B in the CNO structure and the specific capacitance. As shown in Figure 8b, the specific capacitances of B-doped CNOs are 2 (3B-CNOs), 22 (2B-CNOs), and 31 F g$^{-1}$ (1B-CNOs) at 1 mV s$^{-1}$. The first interesting observation is an enhancement of the specific capacitance of the CNO materials, from 22 F g$^{-1}$ found for the pristine CNOs to 31 F g$^{-1}$ for the B-doped CNs (1B-CNOs in acidic media). This is in good agreement with a previous report on B-doped graphenes exhibiting higher capacitance than their undoped counterparts, owing to the modification of their electron donor/acceptor properties.[63] The observation is also consistent with the fact that the B-doped CNOs exhibited a wider pore-size distribution in comparison with the pristine carbon nanoparticles (Table 3). This possibly increased the accessibility of the ions. Doping with B was also responsible for the formation of defects (Table 2), which in turn could participate in electro-adsorption of ions from the electrolyte. The specific capacitance values obtained from the CVs are in good agreement with those obtained from EIS (Figure 8c). The best performance was observed for the supercapacitors based on the 1B-CNOs sample. The specific capacitance increased with decreasing frequency and reached a value of 27 F g$^{-1}$.

Figure 8d shows the charge–discharge curves of pristine and B-doped CNOs at a current density of 100 mA g$^{-1}$. These reasonably symmetric and linear curves indicate good capacitive behavior. It should be noted that the specific capacitance of 1B-CNOs was 27 F g$^{-1}$ at 0.1 A g$^{-1}$, which agrees well with the results obtained by CV and EIS. Moreover, the specific capacitance of 1B-CNOs remained at 13 F g$^{-1}$ even at a loading current density of 10 A g$^{-1}$ (Figure 8e).

The Ragone plots of pristine and B-doped CNOs shown in Figure 8f illustrate the corresponding specific energy/power densities. As the power density increased from 20 (0.1 A g$^{-1}$) to 4900 W kg$^{-1}$ (30 A g$^{-1}$) for 1B-CNOs and from 20 (0.1 A g$^{-1}$) to 980 W kg$^{-1}$ (5 A g$^{-1}$) for CNOs, the energy densities decreased more slowly for 1B-CNOs. In fact, the energy density of 1B-CNOs calculated at 0.1 A g$^{-1}$ was 0.59 Wh kg$^{-1}$, higher than that of the pristine CNOs (0.44 Wh kg$^{-1}$). These results indicate that the B-doped CNs exhibit good power characteristics.

Analysis of the specific capacitances shows that B-doping changes the electrochemical properties of the supercapacitors (ca. 30% increase of capacitance). Our results indicate that B-doped nanostructures exhibit excellent cycling stability and good power characteristics when used as electrode materials in supercapacitors. Finally, it should be noted that B doping is a promising alternative for the design of supercapacitors as well as for the development of new materials used for construction of energy-storage devices.

## Conclusion

We have shown that annealing nanodiamond (ND) particles under an inert He atmosphere in the presence of B resulted in the formation of polygonal B-doped carbon nano-onions (CNOs). X-ray photoelectron spectroscopy (XPS) and $^{10}$B and $^{11}$B solid-state magic-angle spinning (MAS) NMR results indicated that a wide range of doping levels could be achieved simply by changing the mass ratio of NDs to B. A limited amount of B species could be incorporated into the CNO structure (max. $\approx$3.21 at.%) during the transformation period. TEM results indicated that crystalline graphitic sheets were formed during the annealing of NDs in the presence of B, and polygonal B-doped CNOs were formed without disruption of their graphitic layers. These analyses also revealed that increased amounts of B doping resulted in decreased interlayer spacing and increased crystallite size of the B-doped carbon structures. Owing to good power characteristics and excellent long-term charge–discharge stability, these B-doped carbon materials are very promising for the development of new electronic devices. Finally, we note that the active sites could also play a vital role in enhancing the catalytic activity of oxygen reduction.

## Experimental Section

### Materials

All chemicals and solvents were commercially available and used without further purification: ND powder (Carbodeon μDiamond®-Molto) with a crystal size between 4–6 nm and ND content larger than 97 wt.%, boron (Aldrich, amorphous powder, submicron), NaCl (ca. 98%, Sigma–Aldrich), and anhydrous ethanol (99.8%, Poch, Poland). All aqueous solutions for electrochemical studies were prepared using deionized water, which was further purified with the Milli-Q system (Millipore).

### Synthesis of pristine CNOs and B-CNOs

**Pristine CNOs**: Commercially available ND powder with a crystal size between 4–6 nm was used for the preparation of CNOs. NDs were placed in a graphite crucible and transferred to an Astro carbonization furnace. The air in the furnace was removed by applying a vacuum followed by purging with He. The process was repeated twice to ensure complete air removal. Annealing of the ultradispersed NDs was performed at 1650 °C under a 1.1 MPa He atmosphere with a heating rate of 20 °C min$^{-1}$.[6,8] The final temperature was maintained for 1 h, then the material was slowly cooled to room temperature over a period of 1 h. The furnace was opened, and the CNOs were annealed in air at 400 °C to remove any amorphous carbon.

**Boron-doped (B-CNOs)**: NDs (500 mg) and B (50, 100, or 250 mg) were placed in a graphite crucible and the same annealing procedure was applied. B-CNO nanostructures with the following mass ratios resulted: $m_{CNOs}/m_B$ [mg mg$^{-1}$] = 500:50 (10:1); 500/100 (5:1); and 500/250 (2:1), labelled as 1B-CNOs, 2B-CNOs, and 3B-CNOs, respectively.

### Methods

The films were imaged by secondary-electron SEM using a FEI Tecnai S-3000N (Tokyo, Japan). The accelerating voltage of the elec-

tron beam was 30 keV. The EDX analyses were performed with the ASPEX System, fully integrated and automated with the SEM.TEM images were recorded using the FEI Tecnai™ G2 20 X-TWIN instrument. The TEM point resolution was 0.25 nm, the TEM line resolution was 0.144 nm, the maximum diffraction angle was $\pm 12^{\circ}$, and the working distance was 10 mm. The accelerating voltage of the electron beam was 200 keV.

Thermogravimetric experiments were performed using a SDT 2960 Simultaneous TGA-DTG (TA Instruments company). The thermogravimetric spectra were recorded at 10 °C min$^{-1}$ in air, Ar, or $O_2$ atmosphere (100 mL min$^{-1}$).

The powder diffraction data were measured at 293 K using a SuperNova diffractometer (Agilent) with a CCD detector and a CuK$\alpha$ radiation source at a 148 mm sample-to-detector distance. Prior to the experiment, all samples were loaded into capillaries with a diameter of 0.5 mm.

$N_2$ gas-adsorption measurements were performed using a Micromeritics apparatus (ASAP2020 automatic sorption analyzer, Micromeritics Corp., USA) at −196 °C. Prior to gas-adsorption analysis, all samples were degassed at 350 °C at 10 μmHg vacuum for 20 h to remove any adsorbed species.

XPS measurements were performed in an ultra-high vacuum (UHV) chamber (base pressure: $6\times10^{-10}$ mbar) using a non-monochromatic AlK$\alpha$ (1486.7 eV) radiation source (VG Scienta SAX 100) and monochromator (VG Scienta XM 780). The AlK$\alpha$ source was operated at 12 kV and 30 mA. For all samples, a low-resolution survey run (0–1200 eV) was performed. The pristine CNO and B-CNO powder samples were placed on naturally oxidized Si wafers (ITME, Poland) precovered with approximately 50 nm of Au (purity 99.999%) using molecular beam epitaxy (MBE) (PREVAC). The measurements were performed at room temperature. The peaks were fitted using the CasaXPS software (Casa Software Ltd).

$^{10}$B and $^{11}$B solid-state MAS NMR spectra were acquired at 53.7 and 160.47 MHz on a Bruker Advance III 500 MHz WB spectrometer, operating at a magnetic field of 11.7 T. $^{11}$B MAS NMR spectra were recorded with short single-pulse excitations of 0.4 μs (250 kHz) and repetition times of 0.1–1 s. The samples were spun in zirconia rotors at 12 kHz. Typically, 8192 transients were acquired for each spectrum. Short pulses were used to obtain quantitative spectra.[64] $^{11}$B chemical shifts are reported in ppm from external 1 M boric acid solution. To estimate the magnitude of quadrupolar effects, a supplementary $^{11}$B MAS NMR spectrum of the 3B-CNOs sample was measured at 96.2 MHz, using the Tecmag Apollo console operating at a magnetic field of 7.0 T. The spinning speed was equal to 11 kHz, and a single 2 μs RF excitation pulse was used, which corresponded to the 45° flip angle for the liquid. 1000 scans were accumulated with a repetition time of 1 s.

Room-temperature Raman spectra in the range between 100 and 3500 cm$^{-1}$ were investigated with a Renishaw Raman InVia Microscope equipped with a high-sensitivity ultra-low-noise CCD detector. The radiation from an Ar ion laser (514 nm) at an incident power of 1.15 mW was used as the excitation source. Raman spectra were acquired with 3 accumulations of 10 s each, 2400 L mm$^{-1}$ grating, and using a 20× objective.

FT-IR spectra were recorded in the range between 4000 and 100 cm$^{-1}$ with a Nicolet 6700 Thermo Scientific spectrometer at room temperature under a $N_2$ atmosphere. The spectra were collected at a resolution of 4 cm$^{-1}$, apodized with a triangular function, and a zero-filling factor of 1 was applied. All spectra were corrected with conventional software to cancel the variation of the analyzed thickness with the wavelength.

For electrochemical studies, the capacitors were assembled in Swagelok®-type cells by using two electrodes and fiber glass material as a separator. The pellets for electrochemical measurements consisted of 85% of the active electrode material, 10% of binder (polyvinylidene fluoride, PVDF Kynar Flex 2801), and 5% of acetylene black (Super C65, IMERYS). The mass of the electrodes was in the range of 8–10 mg, with a geometric surface area of 0.8 cm$^2$. 1 mol dm$^{-3}$ $H_2SO_4$ was used as an electrolyte for electrochemical measurements. All potentials were measured using three-electrode configuration and are reported versus the normal hydrogen electrode (NHE). All capacitors were examined using CV (1–100 mV s$^{-1}$), galvanostatic cycling, and EIS (100 kHz–1 mHz) using a VMP3 Biologic.

The specific capacitances ($C_s$) of the undoped and B-doped CNOs using CV were determined from the following Equation (1):

$$C_S = \frac{\int_{E_2}^{E_1} i(E)\mathrm{d}E}{vm(E_1-E_2)} \quad (1)$$

in which $E_1$ and $E_2$ are the initial and final potentials [V] respectively, the integral term is the integrated current in the potential window, $v$ is sweep rate [V s$^{-1}$], and $m$ is the mass of the active material.

The specific capacitance (per electrode) was also evaluated by galvanostatic charge–discharge measurements, based on Equation (2):

$$C_S = \frac{2I\Delta t}{m\Delta U} \quad (2)$$

in which $I$ [mA] is the current, $\Delta t$ [s] is the time elapsed for the discharge cycle, $m$ [mg] is the weight of the active electrode material, and $\Delta U$ [V] is the voltage reduced by Ohmic drop.

To determine the electrochemical performance of B-doped materials, the energy density and power density were estimated by using the following Equations (3) and (4):

$$E = \frac{C_S(\Delta U)^2}{2} \quad (3)$$

$$P = \frac{E}{\Delta t} \quad (4)$$

in which $C_s$ [F g$^{-1}$] is the measured device capacitance, $\Delta U$ [V] is the voltage change within the discharge time $\Delta t$ [s], $E$ [Wh kg$^{-1}$] is the energy density, and $P$ [W kg$^{-1}$] corresponds to the average power density.

## Acknowledgements

We gratefully acknowledge the financial support of the National Science Centre, Poland (grant #2012/05/E/ST5/03800) to M.E.P.-B. L.E. thanks the Robert A. Welch Foundation for an endowed chair, grant #AH-0033 and the US NSF, grants: PREM program (DMR-1205302) and CHE-1408865. B.S. gratefully acknowledges the Ministry of Science and Higher Education for the solid-state NMR 500 MHz spectrometer investment Grant (project No. 75/E-68/S/2008-2). SEM, TEM, AUTOLAB, XRD, porosimeter, Raman, and FTIR were funded by European Funds for Regional Development and National Funds of Ministry of Science and Higher Education, as part of the Operational Programme Development of Eastern Poland 2007–2013, projects: POPW.01.03.00-20-034/09 and POPW.01.03.00-20-004/11.

## Conflict of interest

The authors declare no conflict of interest.

**Keywords:** boron · carbon nano-onion · doping · electrochemistry · supercapacitors

[1] R. Bacon, *J. Appl. Phys.* **1960**, *31*, 283.
[2] V. L. Kuznetsov, A. L. Chuvilin, Y. V. Butenko, I. Y. Mal′kov, V. M. Titov, *Chem. Phys. Lett.* **1994**, *222*, 343.
[3] J. K. McDonough, A. I. Frolov, V. Presser, J. Niu, C. H. Miller, T. Ubieto, M. V. Fedorov, Y. Gogotsi, *Carbon* **2012**, *50*, 3298.
[4] M.-S. Wang, D. Golberg, Y. Bando, *ACS Nano* **2010**, *4*, 4396.
[5] M. E. Plonska-Brzezinska, L. Echegoyen, *J. Mater. Chem. A* **2013**, *1*, 13703.
[6] M. E. Plonska-Brzezinska, A. Palkar, K. Winkler, L. Echegoyen, *Electrochem. Solid-State Lett.* **2010**, *13*, K35.
[7] D.. Zhong, H. Sano, Y. Uchiyama, K. Kobayashi, *Carbon* **2000**, *38*, 1199.
[8] Y. Liu, D. Y. Kim, *Electrochim. Acta* **2014**, *139*, 82.
[9] Y. Zhao, C. Hu, Y. Hu, H. Cheng, G. Shi, L. Qu, *Angew. Chem. Int. Ed.* **2012**, *51*, 11371; *Angew. Chem.* **2012**, *124*, 11533.
[10] O. Stephan, P. M. Ajayan, C. Colliex, P. Redlich, J. M. Lambert, P. Bernier, P. Lefin, *Science* **1994**, *266*, 1683.
[11] S. Saito, *Science* **1997**, *278*, 77.
[12] P. Ayala, R. Arenal, A. Loiseau, A. Rubio, T. Pichler, *Rev. Mod. Phys.* **2010**, *82*, 1843.
[13] K. Sasaki, R. Saito, G. Dresselhaus, M. S. Dresselhaus, H. Farhat, J. Kong, *Phys. Rev. B* **2008**, *77*, 245441.
[14] M. Endo, C. Kim, T. Karaki, Y. Nishimura, M. J. Matthews, S. D. M. Brown, M. S. Dresselhaus, *Carbon* **1999**, *37*, 561.
[15] R. B. Sharma, D. J. Late, D. S. Joag, A. Govindaraj, C. N. R. Rao, *Chem. Phys. Lett.* **2006**, *428*, 102.
[16] N. Murata, J. Haruyama, J. Reppert, A. M. Rao, T. Koretsune, S. Saito, M. Matsudaira, Y. Yagi, *Phys. Rev. Lett.* **2008**, *101*, 027002.
[17] T. Soga, T. Kokubu, Y. Hayashi, T. Jimbo, *Thin Solid Films* **2005**, *482*, 86.
[18] J. Ozaki, N. Kimura, T. Anahara, A. Oya, *Carbon* **2007**, *45*, 1847.
[19] J. A. Talla, *Phys. B* **2012**, *407*, 966.
[20] Y. Lin, X. Pan, W. Qi, B. Zhang, D. S. Su, *J. Mater. Chem. A* **2014**, *2*, 12475.
[21] J. Bartelmess, E. De Luca, A. Signorelli, M. Baldrighi, M. Becce, R. Brescia, V. Nardone, E. Parisini, L. Echegoyen, P. P. Pompa, S. Giordani, *Nanoscale* **2014**, *6*, 13761.
[22] Y. Lin, Y. Zhu, B. Zhang, Y. A. Kim, M. Endo, D. S. Su, *J. Mater. Chem. A* **2015**, *3*, 21805.
[23] S. Iijima, *J. Cryst. Growth* **1980**, *50*, 675.
[24] C. Jin, K. Suenaga, S. Iijima, *J. Phys. Chem. C* **2009**, *113*, 5043.
[25] H. W. Kroto, *Nature* **1992**, *359*, 670.
[26] A. Molina-Ontoria, M. N. Chaur, M. E. Plonska-Brzezinska, L. Echegoyen, *Chem. Commun.* **2013**, *49*, 2406.
[27] D. Golberg, Y. Bando, K. Kurashima, T. Sasaki, *Carbon* **1999**, *37*, 293.
[28] S. Tomita, M. Fujii, S. Hayashi, *Phys. Rev. B* **2002**, *66*, 245424.
[29] S. Tomita, A. Burian, J. C. Dore, D. LeBolloch, M. Fujii, S. Hayashi, *Carbon* **2002**, *40*, 1469.
[30] A. E. Aleksenskii, M. V. Baidakova, A. Y. Vul", V. Y. Davydov, Y. A. Pevtsova, *Phys. Solid State* **1997**, *39*, 1007.
[31] Q.-H. Yang, P.-X. Hou, M. Unno, S. Yamauchi, R. Saito, T. Kyotani, *Nano Lett.* **2005**, *5*, 2465.
[32] P. K. Srivastava, *J. Vac. Sci. Technol. Vac. Surf. Films* **1985**, *3*, 2129.
[33] R. D. Allen, *J. Am. Chem. Soc.* **1953**, *75*, 3582.
[34] R. M. Mohanty, K. Balasubramanian, S. K. Seshadri, in *Advances in Ceramics—Characterization, Raw Materials, Processing, Properties, Degradation and Healing* (Ed.: C. Sikalidis), InTech, **2011**.
[35] D. Wei, Y. Liu, Y. Wang, H. Zhang, L. Huang, G. Yu, *Nano Lett.* **2009**, *9*, 1752.
[36] A. Dimiev, D. V. Kosynkin, A. Sinitskii, A. Slesarev, Z. Sun, J. M. Tour, *Science* **2011**, *331*, 1168.
[37] Y. A. Kim, K. Fujisawa, H. Muramatsu, T. Hayashi, M. Endo, T. Fujimori, K. Kaneko, M. Terrones, J. Behrends, A. Eckmann, C. Casiraghi, K. S. Novoselov, R. Saito, M. S. Dresselhaus, *ACS Nano* **2012**, *6*, 6293.
[38] Y. H. Xiong, C. S. Xiong, S. Q. Wei, H. W. Yang, Y. T. Mai, W. Xu, S. Yang, G. H. Dai, S. J. Song, J. Xiong, Z. M. Ren, J. Zhang, H. L. Pi, Z. C. Xia, S. L. Yuan, *Appl. Surf. Sci.* **2006**, *253*, 2515.
[39] Z.-H. Sheng, H.-L. Gao, W.-J. Bao, F.-B. Wang, X.-H. Xia, *J. Mater. Chem.* **2012**, *22*, 390.
[40] C. L. Turner, R. E. Taylor, R. B. Kaner, *J. Phys. Chem. C* **2015**, *119*, 13807.
[41] K. Kanehashi, K. Saito, *J. Mol. Struct.* **2002**, *602–603*, 105.
[42] S.-J. Hwang, C. Fernandez, J. P. Amoureux, J. Cho, S. W. Martin, M. Pruski, *Solid State Nucl. Magn. Reson.* **1997**, *8*, 109.
[43] L.-S. Du, J. F. Stebbins, *Solid State Nucl. Magn. Reson.* **2005**, *27*, 37.
[44] B. Sulikowski, J. Klinowski, in *Zeolite Synthesis Vol. 398* (Eds.: M. L. Occelli, H. E. Robson), American Chemical Society, Washington, DC, **1989**, pp. 393–404.
[45] M. Derewiński, S. Dźwigaj, J. Haber, R. Mostowicz, B. Sulikowski, *Z. Phys. Chem.* **1991**, *171*, 53.
[46] M. Murakami, T. Shimizu, M. Tansho, Y. Takano, S. Ishii, E. A. Ekimov, V. A. Sidorov, K. Takegoshi, *Diamond Relat. Mater.* **2009**, *18*, 1267.
[47] S. Ding, S. Zheng, M. Xie, L. Peng, X. Guo, W. Ding, *Microporous Mesoporous Mater.* **2011**, *142*, 609.
[48] L. S. Panchakarla, A. Govindaraj, C. N. R. Rao, *ACS Nano* **2007**, *1*, 494.
[49] F. Inoue, R. A. Ando, C. M. S. Izumi, P. Corio, *J. Phys. Chem. C* **2014**, *118*, 18240.
[50] S. B. Fagan, A. G. S. Filho, J. M. Filho, P. Corio, M. S. Dresselhaus, *Chem. Phys. Lett.* **2005**, *406*, 54.
[51] K. Chizari, U. Sundararaj, *Mater. Lett.* **2014**, *116*, 289.
[52] T. Sharifi, F. Nitze, H. R. Barzegar, C.-W. Tai, M. Mazurkiewicz, A. Malolepszy, L. Stobinski, T. Wågberg, *Carbon* **2012**, *50*, 3535.
[53] A. C. Ferrari, J. Robertson, *Phys. Rev. B* **2000**, *61*, 14095.
[54] M. I. Baraton, T. Merle, P. Quintard, V. Lorenzelli, *Langmuir* **1993**, *9*, 1486.
[55] T. Takahashi, H. Itoh, M. Kuroda, *J. Cryst. Growth* **1981**, *53*, 418.
[56] F. A. Miller, C. H. Wilkins, *Anal. Chem.* **1952**, *24*, 1253.
[57] K. W. Völger, E. Kroke, C. Gervais, T. Saito, F. Babonneau, R. Riedel, Y. Iwamoto, T. Hirayama, *Chem. Mater.* **2003**, *15*, 755.
[58] S. Baik, J. W. Lee, *RSC Adv.* **2015**, *5*, 24661.
[59] C.-M. Chen, Y.-M. Dai, J. G. Huang, J.-M. Jehng, *Carbon* **2006**, *44*, 1808.
[60] E. Frackowiak, F. Beguin, *Carbon* **2001**, *39*, 937.
[61] E. Frackowiak, *Phys. Chem. Chem. Phys.* **2007**, *9*, 1774.
[62] S. Brunauer, P. H. Emmett, E. Teller, *J. Am. Chem. Soc.* **1938**, *60*, 309.
[63] J. Han, L. L. Zhang, S. Lee, J. Oh, K.-S. Lee, J. R. Potts, J. Ji, X. Zhao, R. S. Ruoff, S. Park, *ACS Nano* **2013**, *7*, 19.
[64] P. P. Man, J. Klinowski, *Chem. Phys. Lett.* **1988**, *147*, 581.

Manuscript received: February 28, 2017
Accepted Article published: March 24, 2017
Final Article published: April 26, 2017